AMERICAN SOCIETY FOR MICROBIOLOGY | Journal of Virology

Virology | Full-Length Text

Adaptation of SARS-CoV-2 to ACE2$_{H353K}$ mice reveals new spike residues that drive mouse infection

Kun Li,[1] Abhishek Verma,[2] Pengfei Li,[2] Miguel E. Ortiz,[1] Grant M. Hawkins,[3] Nicholas J. Schnicker,[4] Peter J. Szachowicz,[5] Alejandro A. Pezzulo,[5] Christine L. Wohlford-Lenane,[1] Tom Kicmal,[3] David K. Meyerholz,[6] Tom Gallagher,[3] Stanley Perlman,[1,2] Paul B. McCray Jr.[1,2]

AUTHOR AFFILIATIONS See affiliation list on p. 17.

ABSTRACT The Coronavirus Disease 2019 (COVID-19) pandemic continues to cause extraordinary loss of life and economic damage. Animal models of severe acute respiratory syndrome-coronavirus-2 (SARS-CoV-2) infection are needed to better understand disease pathogenesis and evaluate preventive measures and therapies. While mice are widely used to model human disease, mouse angiotensin converting enzyme 2 (ACE2) does not bind the ancestral SARS-CoV-2 spike protein to mediate viral entry. To overcome this limitation, we "humanized" mouse *Ace2* using CRISPR gene editing to introduce a single amino acid substitution, H353K, predicted to facilitate S protein binding. While H353K knockin *Ace2* (mACE2$_{H353K}$) mice supported SARS-CoV-2 infection and replication, they exhibited minimal disease manifestations. Following 30 serial passages of ancestral SARS-CoV-2 in mACE2$_{H353K}$ mice, we generated and cloned a more virulent virus. A single isolate (SARS2$_{MA\text{-}H353K}$) was prepared for detailed studies. In 7–11-month-old mACE2$_{H353K}$ mice, a 10^4 PFU inocula resulted in diffuse alveolar disease manifested as edema, hyaline membrane formation, and interstitial cellular infiltration/thickening. Unexpectedly, the mouse-adapted virus also infected standard BALB/c and C57BL/6 mice and caused severe disease. The mouse-adapted virus acquired five new missense mutations including two in spike (K417E, Q493K), one each in nsp4, nsp9, and M and a single nucleotide change in the 5′ untranslated region. The Q493K spike mutation arose early in serial passage and is predicted to provide affinity-enhancing molecular interactions with mACE2 and further increase the stability and affinity to the receptor. This new model and mouse-adapted virus will be useful to evaluate COVID-19 disease and prophylactic and therapeutic interventions.

IMPORTANCE We developed a new mouse model with a humanized angiotensin converting enzyme 2 (ACE2) locus that preserves native regulatory elements. A single point mutation in mouse ACE2 (H353K) was sufficient to confer *in vivo* infection with ancestral severe acute respiratory syndrome-coronavirus-2 virus. Through *in vivo* serial passage, a virulent mouse-adapted strain was obtained. In aged mACE2H353K mice, the mouse-adapted strain caused diffuse alveolar disease. The mouse-adapted virus also infected standard BALB/c and C57BL/6 mice, causing severe disease. The mouse-adapted virus acquired five new missense mutations including two in spike (K417E, Q493K), one each in nsp4, nsp9, and M and a single nucleotide change in the 5′ untranslated region. The Q493K spike mutation arose early in serial passage and is predicted to provide affinity-enhancing molecular interactions with mACE2 and further increase the stability and affinity to the receptor. This new model and mouse-adapted virus will be useful to evaluate COVID-19 disease and prophylactic and therapeutic interventions.

KEYWORDS SARS-CoV-2, mouse-adapted virus, coronavirus, pathogenesis

Editor Mark T. Heise, University of North Carolina at Chapel Hill, Chapel Hill, North Carolina, USA

Address correspondence to Stanley Perlman, stanley-perlman@uiowa.edu, or Paul B. McCray, paul-mccray@uiowa.edu.

Kun Li, Abhishek Verma, and Pengfei Li contributed equally to this article. The order was decided based on discussions between the co-first authors and Drs. McCray and Perlman.

The authors declare no conflict of interest.

See the funding table on p. 17.

Received 27 September 2023
Accepted 28 November 2023
Published 3 January 2024

[This article was published on 3 January 2024 with Alejandro A. Pezzulo's name misspelled in the byline. The byline was updated in the current version, posted on 23 January 2024.]

SARS-CoV-2 (severe acute respiratory syndrome-coronavirus-2), the cause of the COVID-19 pandemic, continues to circulate throughout the USA and the world. As of 17 November 2023, 771 million infections have been recorded, with 6.9 million associated deaths (https://covid19.who.int). While useful vaccines have been developed, the pathogenesis of the infection is still not well understood, and the number of useful antiviral therapies remains small. For both of these reasons, it is critical that experimental animal models of COVID-19 be developed or refined. Several animals are known to be infectable by SARS-CoV-2 including hamsters, non-human primates, ferrets, and cats (1–3). Mice are not susceptible to infection with ancestral strains of SARS-CoV-2, although they can be infected by several recently identified virus strains, including several variants of concern such as the current Omicron variants. Mouse and human ACE2 (angiotensin converting enzyme 2) are very similar, so that minimal changes in either the virus or mACE2 allow infection by strains, such as the Delta variant, that are unable to use mACE2. Studies showed that only one or two amino acid changes in the SARS-CoV-2 S protein allowed murine infection (4–8), as did murine expression of hACE2, either using transducing viral vectors, transgenically, or after insertion into the mACE2 locus (9–17). Mice transgenically expressing hACE2 have been developed and are widely used, but SARS-CoV-2 infection can cause encephalitis in addition to pneumonia in these animals, which confounds modeling of the respiratory disease (12–14, 18).

None of the approaches in which hACE2 was inserted into the mACE2 locus preserved all of the regulatory features associated with mACE2 expression, since hACE2 cDNAs were inserted into the mACE2 genomic sequence in place of a single exon. Studies would benefit from mice expressing hACE2 in which all putative intron and exon regulatory elements in the gene were preserved. For these reasons, it would be useful to have access to a mouse that expresses hACE2 under the mACE2 promoter. mACE2 and hACE2 are sufficiently homologous such that a single amino acid change in ACE2 at position 353 (H353K) is predicted to confer susceptibility in mice (19).

Here, based on the report of Wan et al. (19), CRISPR/Cas9 endonuclease-mediated genome editing was used to develop a mouse with the H353K mutation in exon 8 of the ACE2 locus on the X chromosome ($mACE2_{H353K}$). We show that this minimal, single amino acid substitution rendered mice sensitive to infection with ancestral SARS-CoV-2. Infected mice developed only mild disease, but virulence was enhanced by virus passage through the lungs of $mACE2_{H353K}$ mice. This mouse-adapted virus could infect standard laboratory mice and, in some cases, cause severe disease, even though it did not encode amino acid substitutions in the spike proteins that are most commonly associated with mouse adaptation.

RESULTS

Development of mice expressing mACE2-H353K

To identify a mACE2 mutation that sensitizes cells for SARS-CoV-2 infection, we developed plasmids encoding wild-type mACE2 and mACE2 with the H353K or A329E mutations, sites of known interactions between human ACE2 and the SARS-CoV-2 S protein RBD (4, 19). We transfected these plasmids into 293T cells, which are intrinsically resistant to SARS-CoV-2 infection and demonstrated that mACE2-H353K, but not mACE2 or mACE2-A329E, sensitized cells for infection by pseudoviruses expressing the ancestral SARS-CoV-2 S protein with or without a C-terminal C9 epitope tag (Fig. 1A). All the plasmids expressed their protein products at similar abundance as assessed by immunoblot (Fig. 1B). Based on these findings, a mouse was developed using CRISPR/Cas gene targeting technology to encode mACE2-H353K on the C57BL/6 background (performed by Jackson Laboratories, see details in Materials and Methods). The resultant mice were viable with no obvious defects in survival or growth. Next, we infected these mice with an ancestral strain of SARS-CoV-2 (USA-WA1/2020, MN985325.1). These mice were susceptible to the virus but developed minimal clinical disease and no mortality (Fig. 2A, B , P0).

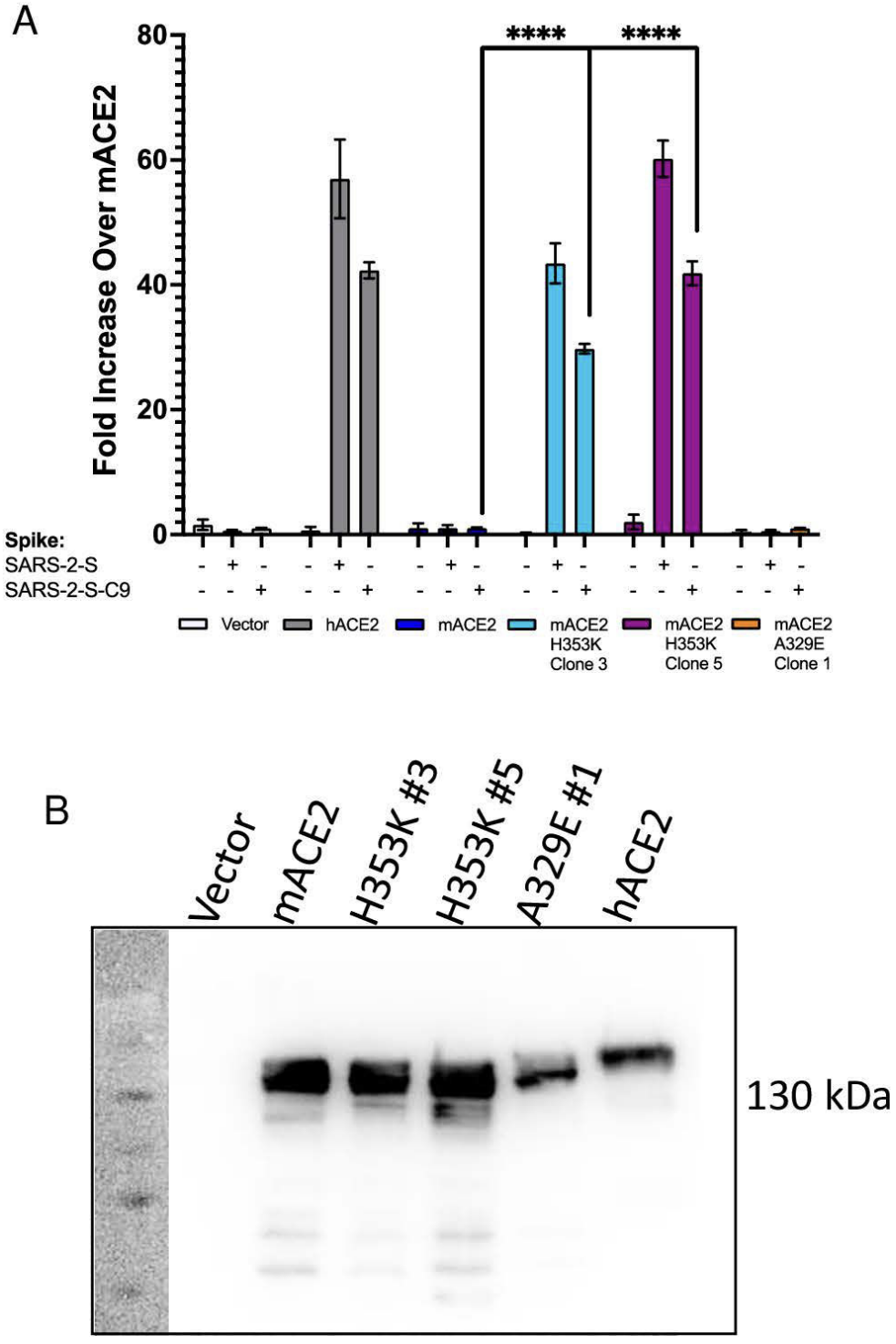

FIG 1 H353K mutation in mACE2 sensitizes cells for infection by ancestral strain. (A) 293T cells were transfected with the corresponding wild-type human (hACE2), mouse ACE2 (mACE2), or mutant mouse ACE2 (mACE2 H353K Clones 3 or 5, mACE2 A329E Clone 1) receptor constructs. At 24 h post-transfection, VSVΔG pseudoviruses containing a Firefly luciferase reporter and the SARS spike protein of interest were used to transduce the transfected 293T cells. Firefly luciferase levels were measured at 18 hr post-transduction. Data (relative luciferase light units) were normalized to mACE2. Complete SARS-2 S proteins were compared with SARS-2 S proteins bearing C-terminal C9 epitope tags (S-C9). Following luciferase measurements, cell lysates from four replicates were pooled together and used to measure ACE2 levels by western blotting (B).

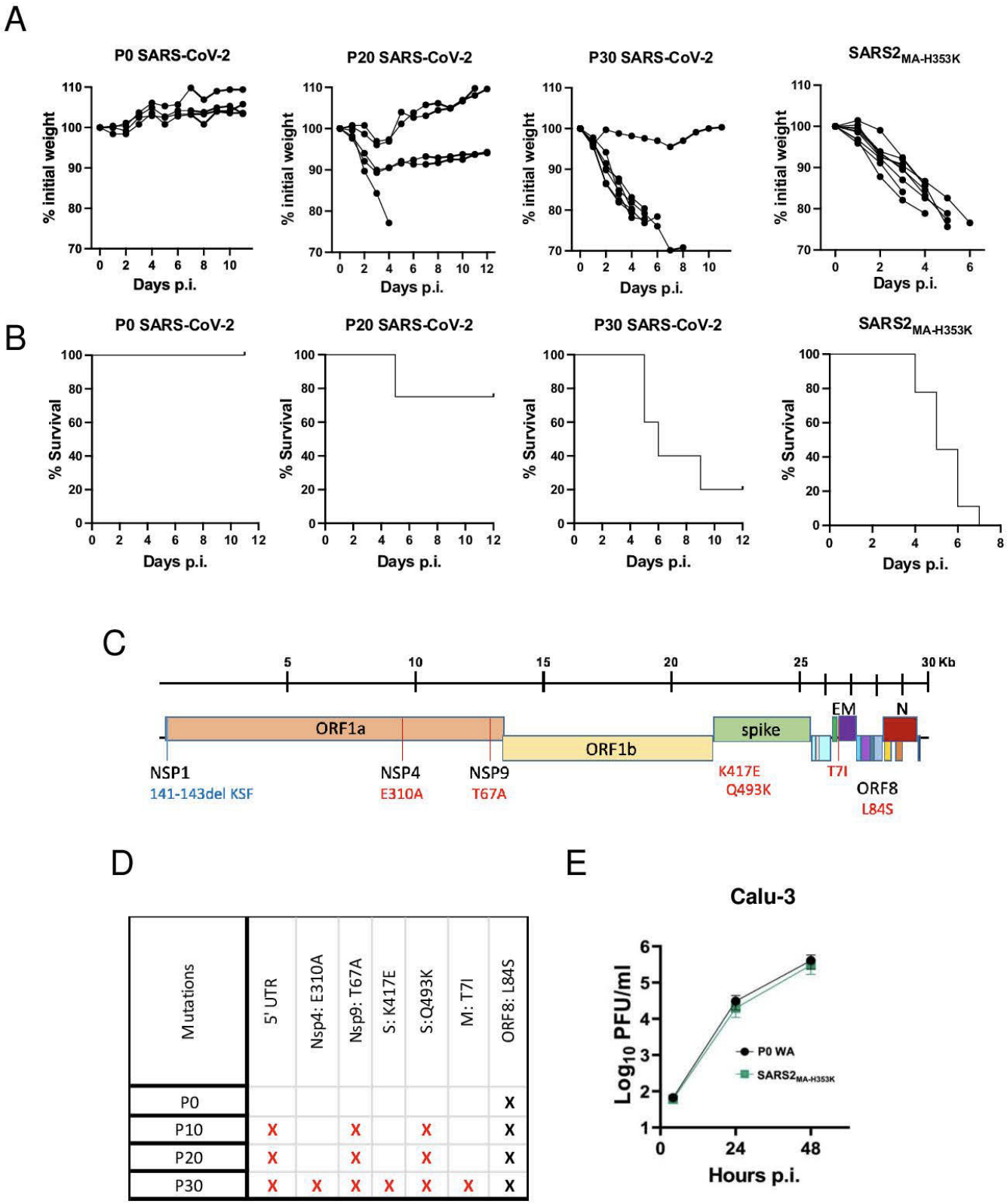

FIG 2 Passage of SARS-CoV-2 in H353K mice. Mice were infected with 4×10^5 PFU of P0 (n = 4), P20 (n = 5), P30 (n = 7), or $SARS2_{MA\text{-}H353K}$ (n = 9) intranasally. (A, B) Weight loss and survival were monitored. (C) Schematic showing SARS-CoV-2 genome of SARS-CoV-2 with mutations indicated in red. (D) Summary of mutations that emerged over passage is shown. (E) Comparison of titers of P0 ancestral strain and $SARS2_{MA\text{-}H353K}$ after growth in Calu-3 cells. Data were acquired from two independent experiments.

Isolation of mouse-adapted SARS-CoV-2

As mACE2$_{H353K}$ mice infected with ancestral SARS-CoV-2 developed only mild disease, we next generated a model for more severe COVID-19 by passaging virus 30 times through mouse lungs. This approach was successfully used previously to generate coronaviruses with increased disease severity in mice (8, 20–22). To assess changes in virulence arising during serial passage, mice were infected with passage 20 (P20) and P30 viruses (Fig. 2A and B). We observed mild disease in mice infected with P20 virus, while mice infected with P30 developed severe clinical disease with substantial weight loss and mortality. We plaque purified P30 viruses and characterized several isolates. We selected a single variant, termed clone SARS2$_{MA-H353K}$, for further study. First, we examined ancestral and SARS2$_{MA-H353K}$ virus growth in a human lung-derived tissue culture cells (Calu-3 cells). These viruses replicated equivalently in Calu-3 cells (Fig. 2E).

Relative to the ancestral virus, SARS2$_{MA-H353K}$ had mutations in the 5′ untranslated region (UTR) and in nsp4, nsp9, and S open reading frames (Fig. 2C and D). We focused on the two missense mutations in the spike protein (Q493K and K417E). Molecular modeling predicts that K353 in mACE2 establishes new hydrogen bonds with the G496 backbone carbonyl and Q498 in the spike protein that are not possible with H353 in mACE2, increasing affinity and stability of the S:mACE2$_{H353K}$ complex (Fig. 3A and B). The spike mutation Q493K appeared after 10 passages through mouse lungs, and it replaces a hydrogen bond between Q493 in the spike and D38 in mACE2 with a stronger salt bridge to the same mACE2 residue, again increasing affinity and stability of the spike protein interactions with both mACE2 and mACE2$_{H353K}$. Similar mutations in spike residue 493 were described in other models of mouse-adapted SARS-CoV-2 (6, 20, 21, 23, 24). Residue 417 in the spike does not interact directly with mACE2, and therefore, K417E does not seem to have an important impact on the affinity and stability of interactions with mACE2. However, mutations in residue 417 are present in human variants of concern B.1.351 (20H/501Y.V2), P.1 (20J/501Y.V3), and several Omicron variants of concern (VOCs), as well as in other mouse-adapted viruses (20, 23). Mutations in residue 417 have been shown to decrease viral neutralization mediated by antibodies (25), but this does not seem relevant to mouse adaptation.

To investigate the effects of the 417 and 493 substitutions on SARS-CoV-2 entry, we adopted the SARS2 VLP assays of Syed et al. (26), as this system closely reflects authentic virus assembly and entry. Nanoluciferase mRNA-containing VLPs with Q493K, K417E, and Q493K/K417E were produced in 293T cells, and the VLPs were harvested from the media, purified, and quantified using established methods (27). We found that the spike substitutions effected no changes to particle assembly and secretion from the producer cells (Fig. S1). We then measured transduction of Nluc mRNAs by the VLPs, using HeLa cells expressing human and mouse ACE2 receptors as targets. As HeLa cells lack SARS-CoV-2-activating proteases, we used trypsin or TMPRSS2 to trigger spike-mediated membrane fusion and subsequent cytoplasmic entry of Nluc mRNAs. VLPs with the single Q493K substitution were most effective at transducing the HeLa cells; relative to the ancestral VLPs, those with Q493K were two- to fourfold more effective at transducing the mACE2-H353K cells (Fig. 3C and D). This finding highlighted the 493 change as central in murine adaptation. However, the K417E change did not provide a similar increased cell entry; in fact, its addition to Q493K VLPs reduced entry to the level of the ancestral VLPs (Fig. 3C and D). During murine adaptation, the K417E change arose after Q493K (Fig. 2D) and was correlated with increased virulence (Fig. 2B). Together with the evidence that residue 493, but not 417, contacts ACE2 residues (Fig. 3A), these findings highlight the K417E change in affecting a biologically significant alteration in cell entry or virus virulence, although the mechanism is not evident. A favored model is that K417E alters spike-mediated virus-cell membrane fusions that take place after ACE2 binding, in ways that decrease *in vitro* virus entry signals yet facilitate *in vivo* mouse lung infection levels. There are several documented spike variations that concomitantly control both membrane fusion and pathogenesis (28, 29). Other mutations that arose during serial passage may also make contributions to virulence and are reviewed in Discussion.

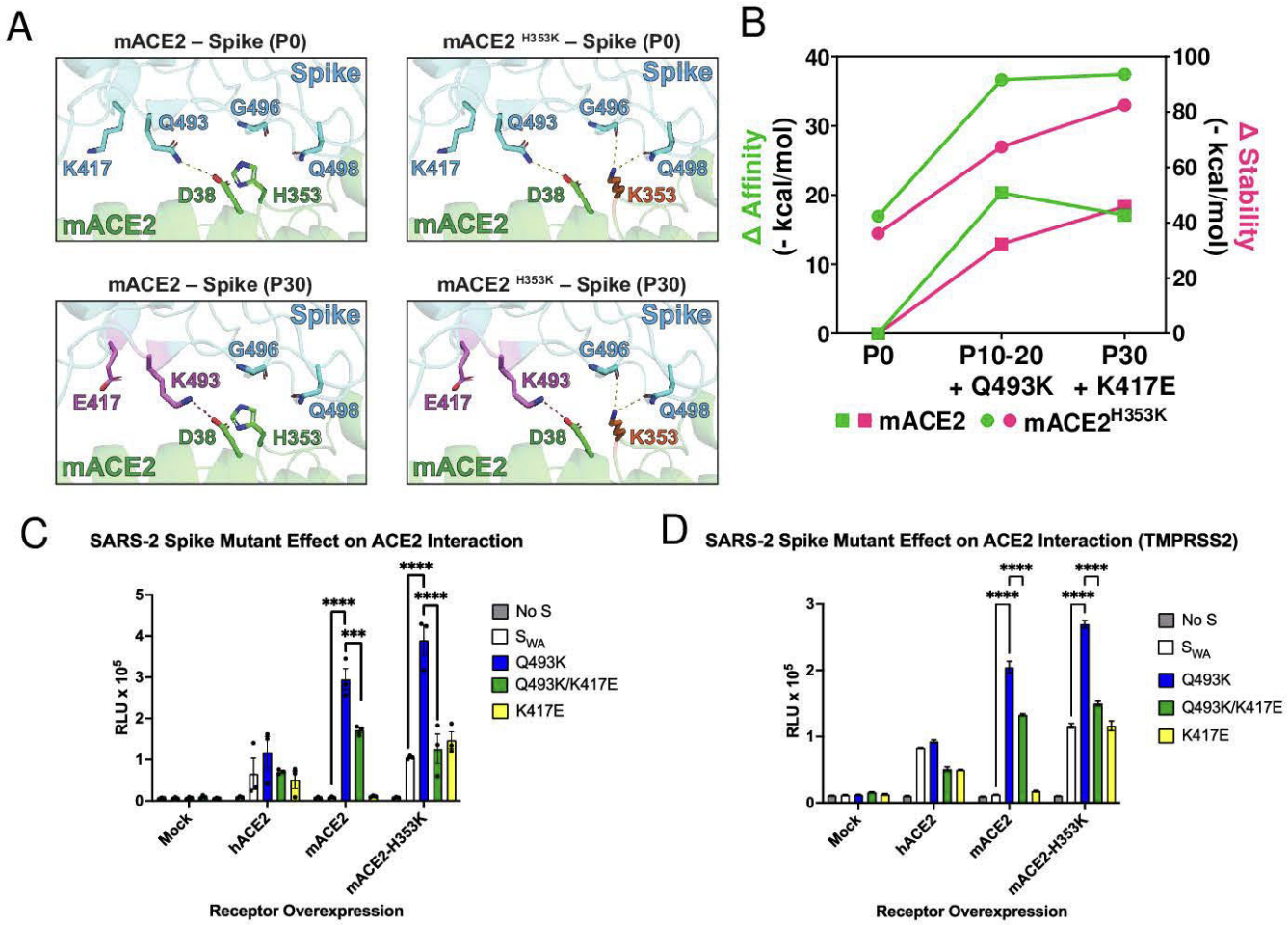

FIG 3 Interactions between ACE2 and SARS-CoV-2 spike protein. (A) *In silico* modeling of the receptor-binding interface between the S protein of 2019-nCoV/USA-WA1/2020 (P0) and $SARS2_{MA\text{-}H353K}$ (P30) with mACE2 (left) and $mACE2_{H353K}$ (right) reveals critical interactions mediated by alterations that emerged through serial passaging. (B) *In silico* modeling of the stability and affinity of S protein binding to mACE2. (C) Relative efficiencies of virus-like particle (VLP) transduction into ACE2-expressing cells. HeLa cells transfected with the indicated ACE2-expressing plasmids were transduced with SARS-CoV-2 VLPs bearing ancestral and mouse-adapted S proteins. S-directed transductions were triggered by exogenous trypsin addition. Nanoluciferase (Nluc) reporter accumulations were measured at 16 hr post-transduction using luminometry. S_{WA} refers to the Washington strain (USA/WA1/2020). (D) Relative efficiencies of VLP transduction into ACE2-expressing cells. HeLa cells co-transfected with TMPRSS2 and the indicated ACE2-expressing plasmids were transduced with SARS-CoV-2 VLPs bearing ancestral and mouse-adapted S proteins. Nanoluciferase reporter accumulations were measured at 16 hr post-transduction using luminometry.

Mouse infection with $SARS2_{MA\text{-}H353K}$

$SARS2_{MA\text{-}H353K}$ caused severe disease and lethality in 7–11-month-old mice after intranasal administration of 10^4 PFU (Fig. 2A and B). We next determined virus titers in the lungs, heart, and brain in 9–11-month-old $mACE2_{H353K}$ mice. We detected peak virus titers in the lungs at 1 day post infection (d.p.i.). Virus was detected in the brain at low levels at 1 d.p.i. but not at later times p.i. Virus was not found in the heart at any time point (Fig. 4A). Next, we assessed the distribution of viral antigen in the lungs using immunohistochemistry. Viral antigen was detected primarily in the airways at day 1 p.i., with spread to the alveoli at days 3 and 5 p.i. (Fig. 4B and C). Histopathological analysis of lungs revealed progressive interstitial lung inflammation with localized lung injury characterized by hyaline membrane formation, perivascular aggregates, and interstitial disease (Fig. 4D). These findings are further summarized in the histopathological scoring shown in Fig. 4E.

As young mice (and young humans) are more resistant to SARS-CoV-2 (20, 30–35), we next infected 9–11-week-old $mACE2_{H353K}$ mice intranasally with 10^4 PFU $SARS2_{MA\text{-}H353K}$.

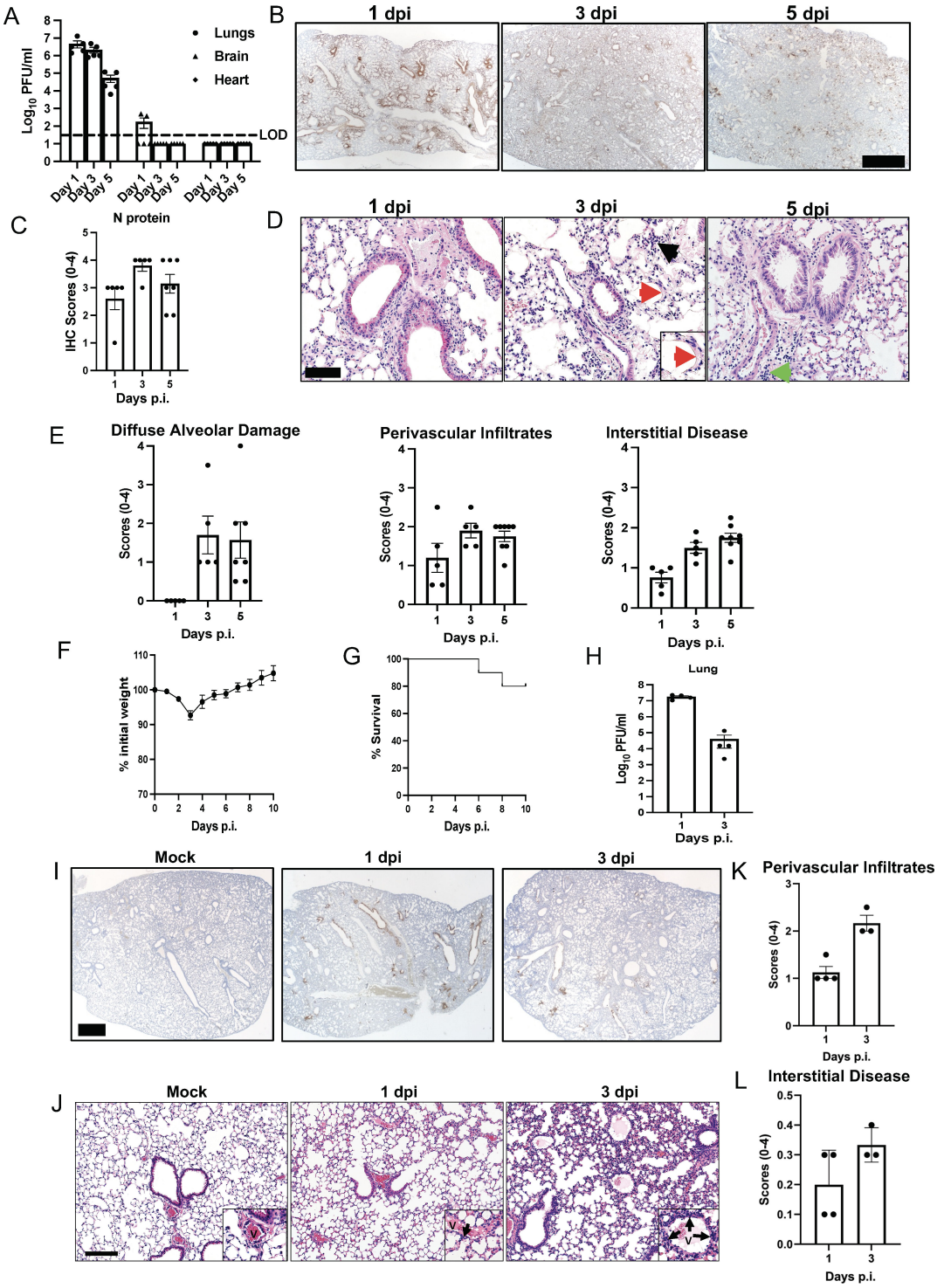

FIG 4 Virus replication and pathological changes in $SARS2_{MA\text{-}H353K}$-infected mice. (A) Virus titers in lungs, brains, and hearts of $SARS2_{MA\text{-}H353K}$-infected 7–11-month-old $mACE2_{H353K}$ mice. (B) Immunohistochemistry staining shows N protein staining in airway and alveoli of lungs. Scale bar represents 730 µm. (C) Summary data showing IHC scores. (D) Histopathological analysis of lungs at 1, 3, and 5 d.p.i. from $SARS2_{MA\text{-}H353K}$-infected mice; scale bar represents 100 µm. Note the morphological examples of hyaline membranes (red arrows and inset), perivascular aggregates (green arrow), and interstitial disease (black arrow). (E) Summary scoring data for effusive diffuse alveolar damage (DAD, e.g., hyaline membranes or edema), perivascular aggregates, and interstitial disease are shown. Data were acquired from two independent sets (n = 5–8 mice). (F through I) Nine- to twelve-week-old $mACE2_{H353K}$ were infected with $SARS2_{MA\text{-}H353K}$ and monitored for survival (F), weight loss (G), virus titers in the lungs (H), and N protein stain (I). Scale bar represents 920 mm. Data are from two independent experiments with 10 mice. (J) Histopathological analysis of lungs at 1 and 3 d.p.i. from $SARS2_{MA\text{-}H353K}$-infected 9–12-week-old mice. Leukocyte infiltration

(Continued on next page)

FIG 4 (Continued)

(arrows, insets) around vessels (V) and interstitial disease scores were generally mild but increased from 1 to 3 d.p.i. Scale bar represents 120 µm. (K, L) Summary scoring data for perivascular aggregates and interstitial disease. Compared with old mice at 1 and 3 d.p.i., the young mice lacked evidence of diffuse alveolar disease and had overall milder disease scores.

Mouse weights were recorded daily. We observed modest weight loss in young mice with a 20% mortality (Fig. 4F and G). As in the older mice, peak virus titers were observed at 1 d.p.i. (Fig. 4H). Notably, titers at day 1 p.i. were equivalent in young and old mACE2$_{H353K}$ mice, even though clinical disease was more apparent in the older animals. Virus was predominantly detected around the airways at day 1 p.i. in young mice (Fig. 4I), as was also observed in older mice (Fig. 4B). Histopathological analysis of lung tissue from young mice inoculated with SARS2$_{MA\text{-}H353K}$ revealed leukocyte infiltration (Fig. 4J, arrows, insets) around vessels (V) and interstitial disease scores that were generally mild but increased from 1 to 3 d.p.i. Compared with old mice at 1 and 3 d.p.i., the young mice lacked detection of diffuse alveolar disease and had overall milder disease scores (Fig. 4K and L). Collectively, these data demonstrate that young and older mACE2$_{H353K}$ mice are similarly susceptible to SARS2$_{MA\text{-}H353K}$ infection but only aged mice develop substantial clinical disease.

SARS2$_{MA\text{-}H353K}$ infection of conventional strains of laboratory mice

The S protein Q493K mutation enhances binding to mACE2-H353K, but structural analyses show that K493 does not directly interact with K353. Further, we detected none of the S protein mutations at positions Q498, P499, or N501 commonly associated with mouse adaptation. Other recent models of SARS-CoV-2 mouse adaptation observed the development of the spike mutations Q493R, Q494H, or Q493K during serial passage, typically in association with mutations at Q498 or N501 (6, 23, 24, 36, 37). Yan and colleagues reported a mouse-adapted strain (MA3) with a single spike mutation Q493R (24). Together, these results suggest that the Q493K mutation might be sufficient for murine infection.

To examine this directly, we next assessed whether SARS2$_{MA\text{-}H353K}$ could infect wild-type BALB/c and C57BL/6 mice. We observed severe weight loss and mortality in 7-month-old BALB/c and C57BL/6 mice infected with SARS2$_{MA\text{-}H353K}$ virus (Fig. 5A and B). We detected high titers of infectious virus in BALB/c mouse lungs, comparable to levels observed in mACE2$_{H353K}$ mice (compare Fig. 4A and 5C). Genomic and subgenomic viral RNA were detected in the lungs and to a lesser extent in the hearts of infected BALB/c mice (Fig. 5D and E). Consistent with these results, viral antigen was detected throughout lung airways and parenchyma (Fig. 5F and G). Histological examination of the lungs revealed extensive edema, which is often associated with poor outcomes in SARS-CoV-2 infections (Fig. 5H and I) (38). In comparing results in wild-type mice with those obtained in mACE2$_{H353K}$ mice, we observed similar morbidity and mortality (Fig. 2A and B vs Fig. 5A and B), similar lung tissue virus titers (Fig. 4A vs Fig. 5C), and similar lung tissue N protein IHC scores (Fig. 4C vs Fig. 5G). We conclude that SARS2$_{MA\text{-}H353K}$ infection caused similar disease severity in wild-type mice and in mACE2$_{H353K}$ mice of similar age.

In general, men develop more severe disease than women (39–42); in parallel, SARS-CoV-2 infection of male mice usually results in increased mortality and morbidity compared with female mice. To assess whether infection with SARS2$_{MA\text{-}H353K}$ also causes more severe disease in males, we infected 7–11-month-old female and male BALB/c mice with 10^3 to 10^5 PFU SARS2$_{MA\text{-}H353K}$. Some or all male mice died after infection at all doses of SARS2$_{MA\text{-}H353K}$, while 7–11-month-old female mice were susceptible only to the highest doses of virus (10^5 PFU) (Fig. 5J, K and L). We measured virus RNA in the lung, brain, liver, kidney, and heart of male and female BALB/c mice 2 d.p.i. (Fig. 5M). We observed no significant differences in the tissue distribution of virus between these groups. To further characterize the lung tissue responses to SARS-CoV-2 infection, we measured the expression of several virus sensors, cytokines, chemokines, and innate immune transcripts 4 d.p.i. by quantitative PCR with reverse transcription (qRT-PCR).

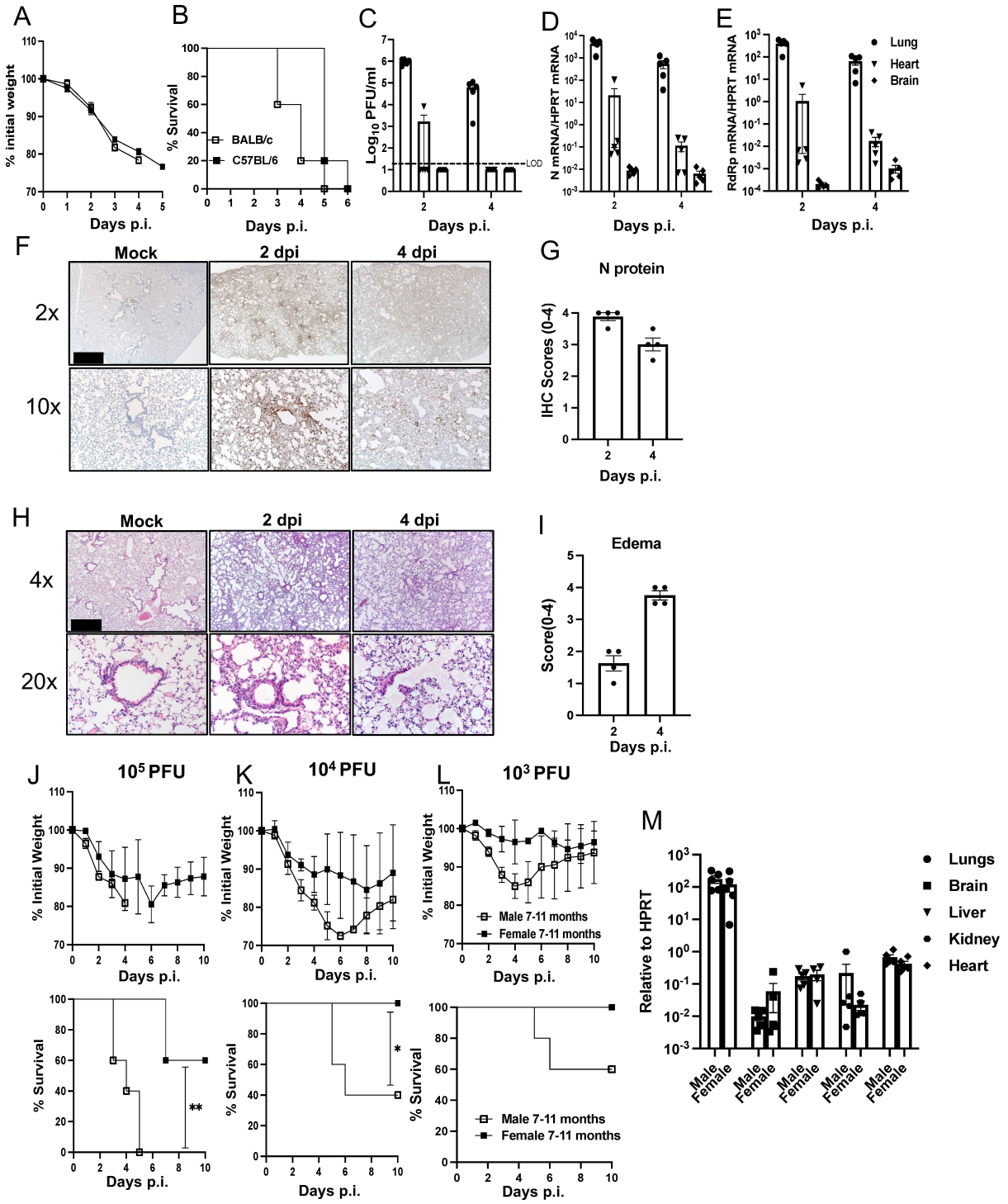

FIG 5 BALB/c and C57BL/6 mice infected with $SARS2_{MA\text{-}H353K}$. Seven- to eleven-month-old C57BL/6 and BALB/c were infected with 4×10^5 PFU of $SARS2_{MA\text{-}H353K}$. (A, B) Weight loss and survival are shown. Data were collected from five mice in two independent experiments. (C through E) Infectious virus titers and N- and RdRp mRNA in lungs, brain, and heart from BALB/c mice were analyzed at 2 and 4 d.p.i. Data were collected from two independent experiments from five mice. (F, G) Immunohistochemical staining for the N protein shows localization of virus in lung parenchyma (F). Scale bar in F represents 1,180 µm. Summary data for IHC scores are shown (G). *n* = 4 mice. (H, I) Histopathological analysis of infected BALB/c mouse lungs at 2, and 4 d.p.i. Scale bar in H represents 590 µm. (J through L) Seven- to eleven-month-old male and female mice were infected with the indicated doses of $SARS2_{MA\text{-}H353K}$ and monitored for survival and weight loss. Data were collected from four to five mice. (M) Viral N gene RNA at 2 d.p.i. in male and female BALB/c mouse lung, brain, heart, kidney, and liver. *n* = 4–5 mice/group.

Compared with infected females, the infected male mice had greater increases in the transcript abundance of MDA5, TNF, CCL2, CXCL2, CXCL9, and CXCL10 (Fig. 6). These responses may have contributed to the worse outcomes in male BALB/c mice.

We also assessed whether young BALB/c mice were more resistant to $SARS2_{MA\text{-}H353K}$, as we observed with young $mACE2_{H353K}$ mice. $SARS2_{MA\text{-}H353K}$-infected 12-week-old BALB/c mice showed minimal weight loss and no mortality after infection (Fig. 7A and B). Consistent with mild disease, the kinetics of virus clearance was more rapid in infected young compared with older mice (compare Fig. 7C and Fig. 5C). In addition, viral antigen was cleared more efficiently from young compared with old BALB/c mice (compare Fig. 5F and G and Fig. 7F and G). Histopathological examination of lungs from young BALB/c mice revealed mild pathological changes at 2 d.p.i. and 4 d.p.i., consisting of modest amounts of edema and inflammatory cell infiltration (Fig. 7D and E).

DISCUSSION

Here, we show that the introduction of a single amino acid substitution in mACE2 ($mACE2_{H353K}$) was sufficient to sensitize mice for infection by ancestral SARS-CoV-2. This adaptation preserved native mACE2 regulatory sequences, facilitating endogenous levels of expression and localization of the protein. In all reported cases, infection of susceptible wild-type mice with human strains of SARS-CoV-2 results in either mild or no disease, with the possible exception of mouse infection with the beta variant, which is occasionally lethal (20, 43, 44). Similarly, when we first infected $mACE2_{H353K}$ mice with SARS-CoV-2, they developed no clinical disease. However, following repeated passage through mouse lungs, the virus became more virulent. A common experience when developing animal models of human coronavirus infection is that the ancestral human virus rarely causes severe disease in the target host. This was observed in mice with SARS-CoV (22) and with MERS-CoV (45). In both settings, serial passage of virus through the lungs yielded a more virulent strain that caused significant morbidity and mortality. This suggests that adaptation to the animal species is required to achieve virulence, and we accomplished this through serial passage.

Two findings related to infection with $SARS2_{MA\text{-}H353K}$ are particularly noteworthy. While young (12-week-old) wild-type BALB/c mice were relatively resistant to infection with $SARS2_{MA\text{-}H353K}$, 7–11-month-old BALB/c mice exhibited significant weight loss and mortality. This result contrasts with our previous findings using the $SARS2\text{-}N501Y_{MA30}$ mouse-adapted strain in BALB/c mice where we observed minimal age variation in response to infection; young BALB/c mice remained susceptible $SARS2\text{-}N501Y_{MA30}$, although at modestly higher doses (46). Leist and colleagues similarly reported that young BALB/c mice were susceptible to severe disease using the MA10 mouse-adapted virus (21). Whether this reflects mouse or virus strain specificity or the lesser virulence of $SARS_{MA\text{-}H353K}$ remains to be determined. Consistent with differences in specificity, following inoculation of 7–11-month-old BALB/c mice with $SARS2_{MA\text{-}H353K}$, we also observed evidence of infection the heart evidenced based on the detection of virus by titer and RNA (Fig. 5C through E). This also contrasts with other reported mouse-adapted viruses (9, 21, 46) where evidence of heart infection is generally absent and may be worthy of additional study related to cardiac involvement during SARS-CoV-2 infection.

Unexpectedly, only two mutations arose in the S protein, both of which have been found in human isolates. Residue 493 was predicted to be critical for ACE2 binding, even as early as in the first few months of the pandemic (19, 47, 48). Notably, Q493K was previously associated with mouse adaptation (6, 20, 21, 49). However, mutations at this site were rarely detected in human isolates prior to the Omicron variants. The other mutation that arose in S, at position 417, is believed to have no effect or a negative effect on virus binding to ACE2, suggesting that the 493 mutation contributes to the gain in virulence. This conclusion is provisional, since we do not know the role of the other $SARS2_{MA\text{-}H353K}$ mutations that occurred in nsp4, nsp9, M, and the 5′ UTR region. It is noteworthy that the virus became markedly more virulent at passage 30 when compared with passage 20, coincident with mutations appearing in nsp4 and M, in addition to

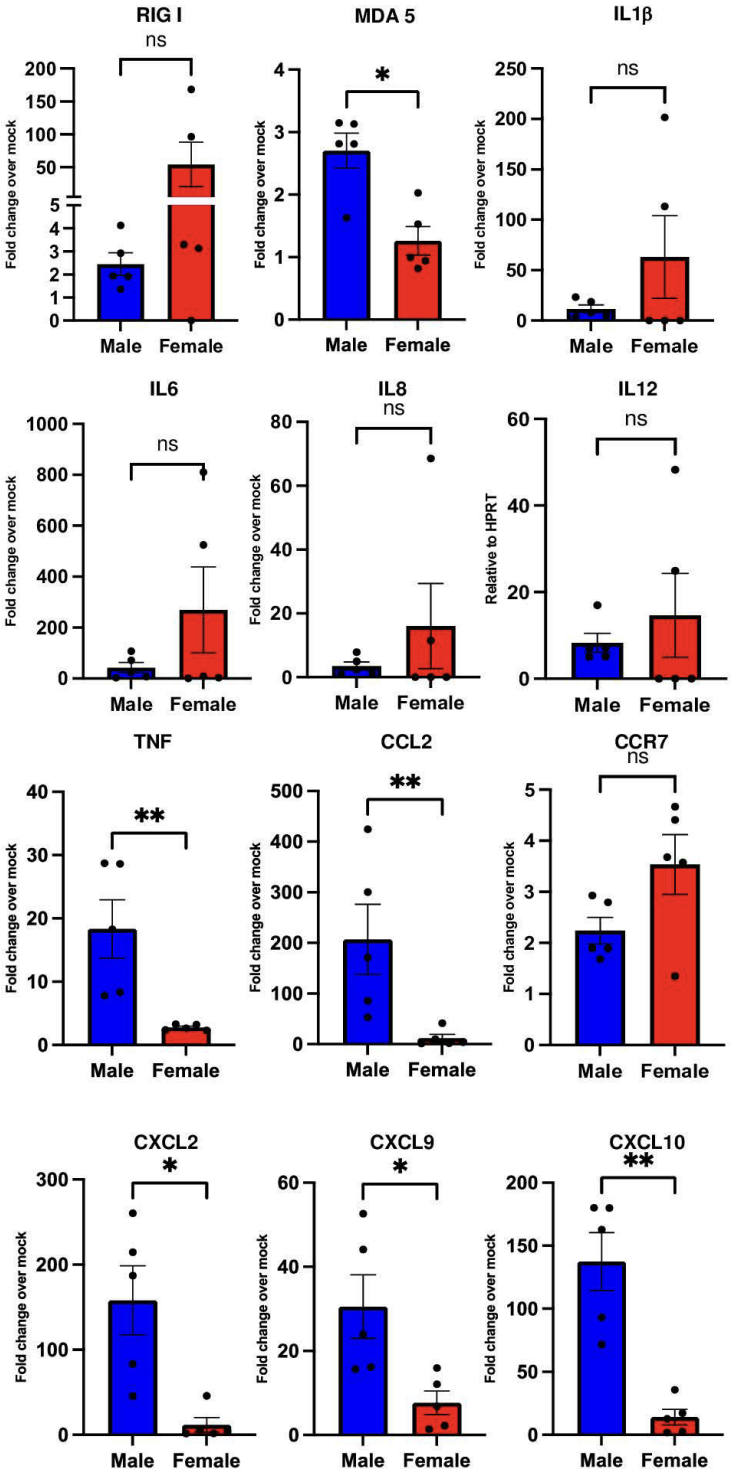

FIG 6 Inflammatory mediators in infected lung tissue. Four days after inoculation with 4×10^5 PFU $SARS2_{MA\text{-}H353K}$, a panel of innate immune effector, cytokine, and chemokine transcripts were measured by qRT-PCR after RNA isolation from lungs of male and female BALB/c mice (7–11 months old). Mock-infected mice serve as controls. Results were expressed as fold change over mock-infected condition (n = 5 mice/group; each lung was collected from an individual mouse). *P < 0.05 and **P < 0.01; ns = not significant. Two-way ANOVA was used to assess statistical significance.

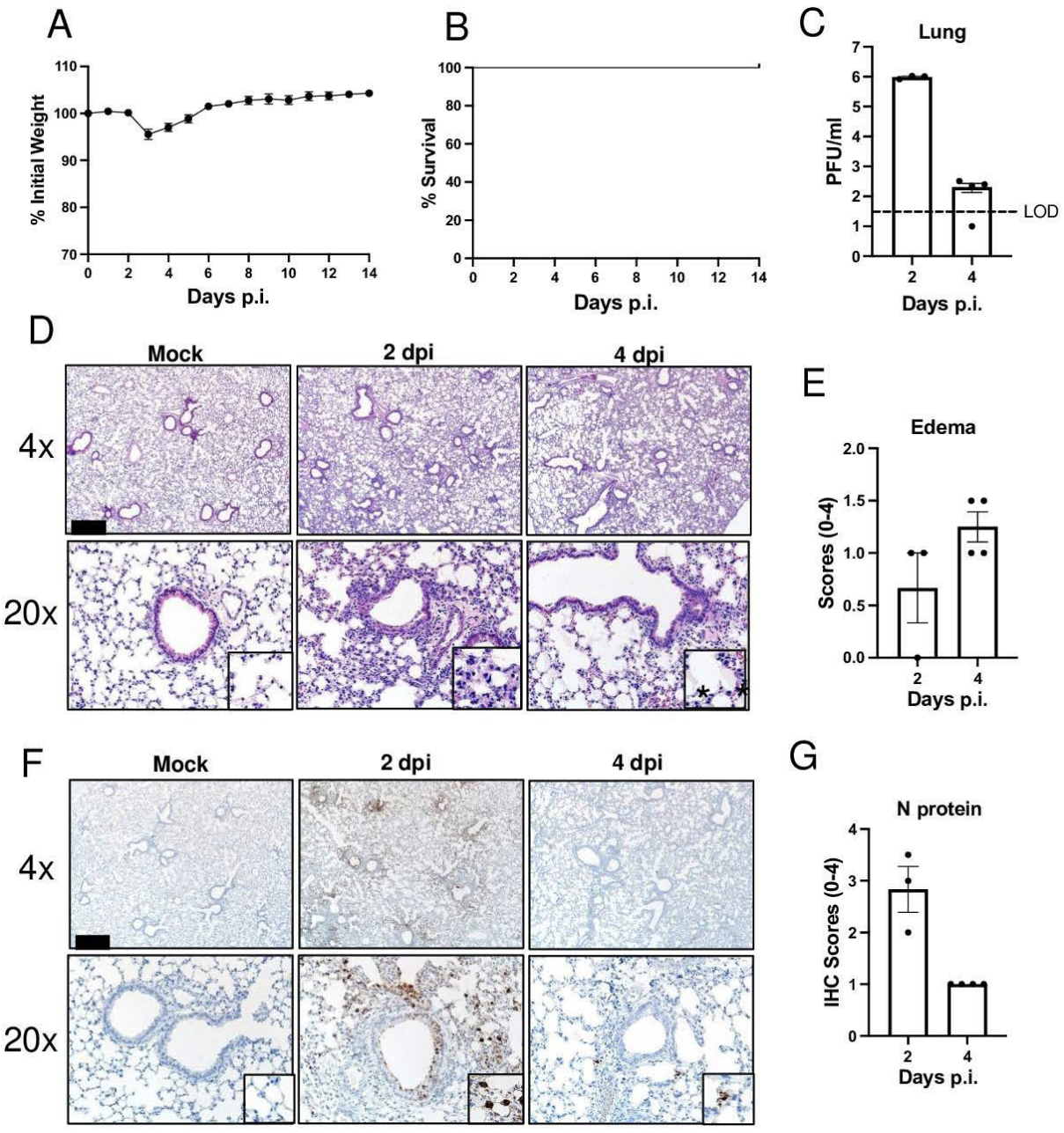

FIG 7 Ten- to twelve-week-old BALB/c mice infected with $SARS2_{MA\text{-}H353K}$. (A, B) BALB/c mice were infected with 5×10^4 PFU $SARS2_{MA\text{-}H353K}$. Weight loss and survival were monitored. (C) Virus titers from lungs were determined at 2 and 4 days p.i., *n* = 3–4 mice. (D, E) Histopathological analysis shows mild edema at 2 and 4 d.p.i. Scale bar in D represents 435 µm. (F, G) Immunostaining for SARS-CoV-2 nucleocapsid in infected lungs was scored using the scoring system in Materials and Methods. Scale bar in F represents 435 µm. Summary data are shown G. *n* = 3–4 mice.

position 417 of the spike protein. One possibility is that the mutation in position 493 is modestly deleterious since it rarely occurs in human isolates and that the 417 mutation compensates for this negative effect of the mutation. In Omicron variants, Q493R was present in the BA.1 and BA.2 and, in agreement with earlier studies, appears to enhance hACE2 binding (Fig. 3A and B) (6, 50, 51). However, Q493 is found in the BA.4, BA.5, and BA.2.75 Omicron subvariants. The K417E mutation and other changes at residue 417 have been associated with evasion of the antibody response, including loss of recognition by several monoclonal antibodies that are used therapeutically, such as REGN10933 (marketed as casirivimab) (52–54). Of note, however, our results indicate that mutations at position 417 are selected in the absence of immune pressure. Further work will be

directed at determining if and how mutations at positions 417 and 493 act together to enhance mouse adaptation and the role of mutations in proteins other than S in SARS-CoV-2 pathogenesis in mice.

Other mutations that arose during *in vivo* serial passage may also contribute to virulence.

Non-structural protein 9 (nsp9) is essential for viral replication, and its sequence is highly conserved in SARS-CoV and SARS-CoV-2. T67A in nsp9 was described in mouse-adapted SARS-CoV (22) and has also occurred in other mouse-adapted SARS-CoV-2 viruses (20, 55), suggesting it is an important mutation for coronavirus adaptation to mice. Δ141–143 in the 5′ UTR sequence and E310A in nsp4 were described in a small number of human samples without any significant associated phenotype. T7I in the membrane protein was reported in another model of SARS-CoV-2 mouse adaptation (56) and was also identified in association with *in vitro* serial passage of the Washington strain (57). In the setting of serial *in vivo* passage in naïve mice, it is unlikely that an anti-virus humoral immune response influenced the outcomes.

Several mouse models of SARS-CoV-2 infection are available including sensitization by transduction with adenoviral or AAV vectors expressing hACE2, transgenic expression of hACE2 with heterologous promoters, and knock in of hACE2 cDNAs or specific point mutations into the mACE2 locus to support virus binding. A study by Winkler et al. used a hACE2 KI C57BL/6 mouse model in which the hACE2 cDNA was inserted in frame with the endogenous initiation codon of the mouse Ace2, preserving mouse Ace2 promoter and enhancer elements (9). In 6-week-old animals, infection with SARS-CoV-2 WA1/2020 or B.1.1.7 or B.1.351 VOCs caused no significant weight loss or mortality, with viral replication predominantly occurring in the nasal turbinates and respiratory tract. While the VOCs contained the N501Y spike mutation, this and other spike mutations were insufficient to drive severe disease manifestations. Nakandakari-Higa and colleagues used CRISPR technology to introduce the H353K, S82M, and F83Y mutations into the C57BL/6J strain (58). While we observed no weight loss in young $ACE2_{H353K}$ mice infected with SARS-CoV-2 WA1/2020 (Fig. 2A), 8–14-week-old Ace2 H353K/S82M/F83Y triple-mutant mice infected with the WA1 strain showed up to 10% wt loss but no mortality, while VOC B.1.1.529 sublineage BA.1 infection caused no significant weight loss (58).

The $ACE2_{H353K}$ mice and the knock in models described above all retained mACE2 native regulatory elements, and all were generated on the C57BL/6 background. We note that disease severity generally increases with age in C57BL/6 mice. Additionally, ancestral strains of SARS-CoV-2 do not cause severe disease manifestations, emphasizing the role of serial passage and mouse adaptation to elicit more robust disease phenotypes. Together, these results emphasize the contributions of mouse strain, age, and sex to disease outcomes. The $ACE2_{H353K}$ model and mouse-adapted $SARS2_{MA\text{-}H353K}$ virus will be useful to investigate SARS-CoV-2 pathogenesis and disease prevention and treatments.

MATERIALS AND METHODS

Cells and virus

Vero-E6, HEK-293T, HEK-293K, and HeLa cells were maintained in Dulbecco's modified Eagle's medium (DMEM, Gibco) containing 10% fetal bovine serum (FBS, Atlanta Biologicals), 10 mM HEPES, 0.1 mM non-essential amino acids, 100 nM sodium pyruvate, and 100 U/mL penicillin and streptomycin (Gibco). Calu-3 2B4 cells were grown in DMEM supplemented with 20% FBS, 10 mM HEPES, 0.1 mM non-essential amino acids, 100 nM sodium pyruvate, and 100 U/mL penicillin and streptomycin. SARS-CoV-2/USA-WA1/2020 (accession number: MN985325.1) (obtained from BEI) was propagated in Calu-3 2B4 and titered in Vero-E6 cells in the BSL-3 facility of the University of Iowa. All cell lines were maintained at 37°C.

Mice

The $mACE_{H353K}$ mice were produced by Jackson Laboratories (Bar Harbor, Maine). An amino acid substitution from Histidine to Lysine (CAC to AAA) at codon 353 in exon 8 of the mACE2 locus on the X chromosome was generated by CRISPR/Cas9 gene editing technology. Guide RNA targeting the region of interest on exon 8 was co-introduced into fertilized eggs using Cas9 endonuclease with pronuclear injection. Embryos were implanted into pseudopregnant recipient females. Correctly targeted pups confirmed by sequencing were further bred for germline transmission. Middle-aged C57BL/6 and BALB/c mice (8–10 months) were purchased from Charles River Laboratories. All mice were maintained and bred in the Animal Care Facility of the University of Iowa. All animal experiments were approved by Institutional Animal Care and Use Committee of the University of Iowa. The $mACE_{H353k}$ mice are available from Jackson Laboratories: Strain #034903, C57BL/6J-*Ace2*^{em1Pbmj}/J.

Pseudovirus production and entry assay

Pseudovirus particles (PPs) based on a VSV packaging system were developed (59). Briefly, HEK-293K cells were transfected with spike protein expression plasmids. After 24 hr, the cells were treated with VSVdeltaG/Junin GP luciferase (VSV-luc PP) for 2 hr. Fresh DMEM with 10% FBS were added to cells after VSV-luc PP was removed. After 48 hr, 72 hr, and 96 hr post-transfection (hptf), cell supernatants were harvested, and debris were removed. PPs were pelleted by low-speed centrifugation through 20% sucrose and then resuspended in DMEM after 100-fold concentration.

HEK-293T cells were transfected with pcDNA3.1 empty plasmid, pcDNA3.1-hACE2, pcDNA3.1-mACE2, pcDNA3.1-$mACE2_{A329E}$ clone 1, pcDNA3.1-$mACE2_{H353K}$ clone 3, or pcDNA3.1-$mACE2_{H353K}$ clone 5. At 2 hrs post-transfection, cells were inoculated with PPs for 6 hr and then replenished with fresh DMEM containing 10% FBS. After 16 hr, cells were lysed in passive 1× lysis buffer (Promega) and then mixed with Firefly luciferase substrate. Relative light units (RLU) were measured using a Veritas microplate luminometer.

VLP production

HEK293T cells at 80% confluence were co-transfected with equimolar

amounts of five plasmids: pcDNA3.1-SARS-CoV-2 S, E, M, and HiBiT-N (60) as well as pcDNA3.1-Nluc-PS9 (26). Plasmid DNAs (20 µg total) were combined with LipoD transfection reagent (SignaGen, Frederick, MD, USA) in serum-free DMEM (SFM), incubated for 10 min, and added dropwise onto 20exp6 cells. At 6 hptf and again at 24 hptf, cells were replenished with fresh DMEM-10% FBS. At 48 hptf, conditioned media were collected, clarified by centrifugation (300 × *g*, 4°C, 10 min; 3,000 × *g*, 4°C, 10 min), and VLPs in media were then purified by equilibrium density gradient ultracentrifugation. Briefly, clarified media were overlaid onto 20% w/wt–50%, wt/wt sucrose cushions (each in SFM-0.1% BSA) and centrifuged at 5°C using a Beckman-Spinco SW28 rotor for 3 hr at 25,000 rpm. Fractions collected from air-gradient interfaces were collected, and VLPs were identified in each fraction by complementation assays. Briefly, 1 µL aliquots of each fraction were mixed with 29 µL 1× Passive Lysis Buffer (Promega) containing 1:200 LgBiT protein (Promega) and 1:200 Nano-Glo luciferase substrate (Promega). HiBiT-N/LgBiT complementation was measured as Nluc RLU using a Veritas microplate luminometer. The VLP-containing fractions were combined and stored in aliquots at −80°C.

VLP transduction

HeLa cells were LipoD transfected with pcDNA3.1-MCS (Mock), pcDNA3.1-hACE2-C9, pCMV3-mACE2, or pCMV3-mACE2-H353K. At 24 hptf, cells were inoculated with VLPs at precisely equivalent HiBiT-N input multiplicities, as measured by HiBiT-N levels in the VLP preparations, and incubated for 2 hr at 37°C. VLPs lacking S proteins (No S)

served as negative controls. At 2 hptd, unadsorbed VLPs were removed and cells were then incubated in fresh DMEM-10% FBS for 16 hr. Media were then removed and cells dissolved into 1× Passive Lysis Buffer (Promega) containing 1:200 Nano-Glo luciferase substrate (Promega). Nluc levels were measured as RLU using a Veritas microplate luminometer.

Western blot

HEK-293T cells were transfected with individual plasmids. At 24 hrs post-transfection, cells were lysed in 1× Laemmli sample buffer and boiled at 95°C for 10 min. Proteins were separated by 8% SDS-PAGE and then transferred to nitrocellulose membranes. Membranes were blocked with 5% non-fat dried milk followed by incubation with the appropriate primary antibodies for 2 hr at room temperature. After being incubated with horseradish peroxidase (HPR)-conjugated secondary antibodies, proteins were visualized using chemiluminescence reagents (Thermo Fisher Scientific).

Serial passage in mice

SARS-CoV-2/USA-WA1/2020 was passaged serially in $mACE_{H353K}$ mice as follows. Two mice were inoculated with 10^5 PFU virus intranasally. Mice were euthanized, and lungs were harvested 2 days post-infection. Mouse lungs were homogenized and freeze thawed once. Homogenates were centrifuged, and supernatants from the two mice were pooled. Fifty microliters of the pooled supernatants was inoculated into two mice intranasally. This process was repeated every 2 days for 30 lung passages. After 30 passages, virus was plaque purified three times in Vero-E6 cells as previously described (20). Purified viruses were propagated in Calu-3 cells and tittered in Vero-E6 cells. All the experiments with SARS-CoV-2 were approved by the University of Iowa Carver College of Medicine BSL3 Oversight Committee. The experiments were conducted in BSL3 facilities that were designed (and annually verified) to conform to the safety requirements recommended by Biosafety in Microbiological and Biomedical Laboratories (BMBL).

Viral genome sequencing

Viral RNA from Calu-3 cell supernatants was isolated using a QIAamp Viral RNA MiniKit (Qiagen) according to manufacturer specifications. Sequencing libraries were prepared following a sequencing protocol (v2) and primer pools (v3) from the ARTIC network (dx.doi.org/10.17504/protocols.io.bdp7i5rn) and were read on a MinION sequencer (Oxford Nanopore Technologies). The consensus sequences were generated using Medaka.

qRT-PCR

Total RNA from tissue was extracted using TRIzol reagent (Thermo Fisher Scientific) following the manufacturer's protocol. After treatment with DNase-I (Thermo Fisher Scientific), 1 µg RNA was used as template for cDNA synthesis. Power SYBR Green PCR Master Mix (Applied Biosystems) was used for real-time quantitative PCR. Ct values were used to calculate the relative abundance of transcripts normalized to HPRT and presented as $2^{-\Delta Ct}$. The primers used to amplify the genomic RNA of the N protein were purchased from integrated DNA technologies (IDT), and the sequences were reported previously (46). The primers used for cytokine and chemokines were reported previously (61). The qPCR primers used in this study are listed in Table 1.

In silico structural modeling and analysis

A homology model for mouse ACE2 (NP_001123985.1) was generated using YASARA and docked into the crystal structure complex of human ACE2 and spike RBD (PDB: 6M0J). Mutation calculations for the mACE2-Spike complex were performed in Bioluminate (Schrodinger Release 2020-4), first using the Protein Preparation Wizard

TABLE 1 qPCR primers

Genes		Sequence (5′–3′)
SARS-CoV-2 RdRp gene	Forward	GGTAACTGGTATGATTTCG
	Reverse	CTGGTCAAGGTTAATATAGG
Mouse HPRT	Forward	GCGTCGTGATTAGCGATGATG
	Reverse	CTCGAGCAAGTCTTTCAGTCC

followed by the Residue Scanning module. Stability and affinity calculations were performed optimizing for the affinity, and backbone minimization was used with a cutoff of 5 Å. Figures were generated in PyMOL. The software used was installed and configured by SBGrid (62).

Infectious virus titers

Mice were euthanized at different times p.i., and organs were collected aseptically into 1× PBS and homogenized. Tissue homogenates were centrifuged, and supernatants were titered by plaque assay on Vero-E6 cells. Briefly, tissue homogenate supernatants were serially diluted 10-fold in DMEM and applied to Vero-E6 cells grown in 12-well dishes. After 30 min, inocula were removed and 1 mL 0.5% agarose containing 2% FBS was overlaid on the cells. After 3 days, the agarose was removed and cells were fixed with 10% formalin for 30 min prior to staining with 0.1% crystal violet. Viral titers were expressed in PFU per mL tissue.

Histology and immunohistochemistry

Mice were euthanized using ketamine-xylazine. Lungs were collected, fixed in zinc formalin (Sigma-Aldrich), and embedded in paraffin. Tissue sections (~4 µm each) were stained with hematoxylin and eosin for routine histology. For immunohistochemistry, sections (~4 µm each) were incubated with a rabbit monoclonal antibody against SARS-CoV-2 N protein (40143-R019, Sino Biological) followed by incubation with Rabbit Envision (Dako) and diaminobenzidine (Dako) as previously described (14). Tissues were examined by a boarded pathologist in a post-examination method of masking and following principles for reproducible tissue scores (63).

Quantitative histomorphometry

Immunostaining of SARS-CoV-2 infection in the lung was scored using distribution-based ordinal scores: 0: absent, 1: <25%; 2: 26%–50%; 3: 51%–75%; and 4: >75% of lung parenchyma. Ordinal scores for markers of diffuse alveolar disease (e.g., edema or hyaline membranes) were assigned on distribution of lung fields (200×) affected: 0: none; 1: <25%; 2: 26%–50%; 3: 51%–75%; and 4: >75% of lung fields. Perivascular/peri-airway lymphoid cell aggregates were scored based on the highest score seen in the lung section: 0: none; 1: scattered solitary cells; 2: small aggregates; 3: small to moderate aggregates cuffing the circumference of the vessel; and 4: large circumferential aggregates that compress adjacent lung tissue. Interstitial disease was evaluated using a modified H-score for interstitial disease: 0: absent; 1: minor increased cellularity in septa; 2: moderate infiltrate septa extending into lumen; and 3: severe infiltrates in septa and lumen ± edema or hyaline membranes. For each grade, the percentage of the affected lung was scored and then multiplied by the grade score. The sum of all grade H-scores was divided by 100 to yield a final score between 0 and 3.

Statistical analysis

Student's *t*-test or ANOVA were used to analyze differences between groups. Statistical significance for survival was analyzed by log-rank (Mantel-Cox) tests. Results are expressed as mean ± SEM. $P < 0.05$ was considered statistically significant. $P < 0.01$ was

considered highly statistically significant. $P < 0.05$ marked as "*," $P < 0.01$ marked as "**," and $P < 0.001$ marked as "***."

ACKNOWLEDGMENTS

This work is supported by the National Institutes of Health (NIH) Grant P01 AI060699 and R01 AI129269 and the Pathology Core, which are partially supported by the Center for Gene Therapy for Cystic Fibrosis (NIH Grant P30 DK-54759), and the Cystic Fibrosis Foundation. P.B.M. is supported by the Roy J. Carver Charitable Trust.

AUTHOR AFFILIATIONS

[1]Department of Pediatrics, The University of Iowa, Iowa City, Iowa, USA
[2]Department of Microbiology and Immunology, The University of Iowa, Iowa City, Iowa, USA
[3]Department of Microbiology and Immunology, Loyola University Chicago, Maywood, Illinois, USA
[4]Protein and Crystallography Facility, The University of Iowa, Iowa City, Iowa, USA
[5]Department of Internal Medicine, The University of Iowa, Iowa City, Iowa, USA
[6]Department of Pathology, The University of Iowa, Iowa City, Iowa, USA

AUTHOR ORCIDs

Kun Li http://orcid.org/0000-0002-8582-2913
Tom Gallagher http://orcid.org/0000-0002-8601-5961
Stanley Perlman http://orcid.org/0000-0003-4213-2354
Paul B. McCray Jr. http://orcid.org/0000-0002-4067-577X

FUNDING

Funder	Grant(s)	Author(s)
HHS | National Institutes of Health (NIH)	P01 AI060699	Stanley Perlman
HHS | National Institutes of Health (NIH)	R01 AI129269	Stanley Perlman

AUTHOR CONTRIBUTIONS

Kun Li, Conceptualization, Investigation, Methodology, Writing – original draft | Abhishek Verma, Investigation, Methodology, Writing – original draft | Pengfei Li, Formal analysis, Investigation, Methodology, Writing – original draft | Miguel E. Ortiz, Formal analysis, Investigation, Methodology, Writing – original draft | Grant M. Hawkins, Formal analysis, Investigation, Methodology, Writing – original draft | Nicholas J. Schnicker, Formal analysis, Investigation, Methodology, Writing – original draft | Peter J. Szachowicz, Formal analysis, Investigation, Methodology, Writing – original draft | Alejandro A. Pezzulo, Data curation, Investigation, Methodology, Writing – original draft | Christine L. Wohlford-Lenane, Investigation, Methodology | Tom Kicmal, Investigation, Methodology | David K. Meyerholz, Formal analysis, Investigation, Methodology, Writing – original draft | Tom Gallagher, Formal analysis, Investigation, Methodology, Writing – original draft | Stanley Perlman, Formal analysis, Funding acquisition, Investigation, Methodology, Writing – original draft | Paul B. McCray Jr., Conceptualization, Funding acquisition, Investigation, Methodology

ADDITIONAL FILES

The following material is available online.

Supplemental Material

Figure S1 (JVI01510-23-S0001.pdf). Characterization of particle assembly and secretion from producer cells.

REFERENCES

1. Chu H, Chan JF-W, Yuen K-Y. 2022. Animal models in SARS-CoV-2 research. Nat Methods 19:392–394. https://doi.org/10.1038/s41592-022-01447-w
2. Shou S, Liu M, Yang Y, Kang N, Song Y, Tan D, Liu N, Wang F, Liu J, Xie Y. 2021. Animal models for COVID-199: hamsters, mouse, ferret, mink, tree shrew, and non-human primates. Front Microbiol 12:626553. https://doi.org/10.3389/fmicb.2021.626553
3. Muñoz-Fontela C, Dowling WE, Funnell SGP, Gsell P-S, Riveros-Balta AX, Albrecht RA, Andersen H, Baric RS, Carroll MW, Cavaleri M, et al. 2020. Animal models for COVID-19. Nature 586:509–515. https://doi.org/10.1038/s41586-020-2787-6
4. Rawle DJ, Le TT, Dumenil T, Yan K, Tang B, Nguyen W, Watterson D, Modhiran N, Hobson-Peters J, Bishop C, Suhrbier A, Lee B. 2021. Ace2-lentiviral transduction enables mouse SARS-CoV-2 infection and mapping of receptor interactions. PLoS Pathog 17:e1009723. https://doi.org/10.1371/journal.ppat.1009723
5. Ren W, Zhu Y, Wang Y, Shi H, Yu Y, Hu G, Feng F, Zhao X, Lan J, Wu J, Kenney DJ, Douam F, Tong Y, Zhong J, Xie Y, Wang X, Yuan Z, Zhou D, Zhang R, Ding Q, Wang D. 2021. Comparative analysis reveals the species-specific genetic determinants of Ace2 required for SARS-CoV-2 entry. PLoS Pathog 17:e1009392. https://doi.org/10.1371/journal.ppat.1009392
6. Huang K, Zhang Y, Hui X, Zhao Y, Gong W, Wang T, Zhang S, Yang Y, Deng F, Zhang Q, Chen X, Yang Y, Sun X, Chen H, Tao YJ, Zou Z, Jin M. 2021. Q493K and Q498H substitutions in spike promote adaptation of SARS-CoV-2 in mice. EBioMedicine 67:103381. https://doi.org/10.1016/j.ebiom.2021.103381
7. Gu H, Chen Q, Yang G, He L, Fan H, Deng Y-Q, Wang Y, Teng Y, Zhao Z, Cui Y, et al. 2020. Adaptation of SARS-CoV-2 in BALB/C mice for testing vaccine efficacy. Science 369:1603–1607. https://doi.org/10.1126/science.abc4730
8. Dinnon KH III, Leist SR, Schäfer A, Edwards CE, Martinez DR, Montgomery SA, West A, Yount BL Jr, Hou YJ, Adams LE, Gully KL, Brown AJ, Huang E, Bryant MD, Choong IC, Glenn JS, Gralinski LE, Sheahan TP, Baric RS. 2020. A mouse-adapted model of SARS-CoV-2 to test COVID-19 countermeasures. Nature 586:560–566. https://doi.org/10.1038/s41586-020-2708-8
9. Winkler ES, Chen RE, Alam F, Yildiz S, Case JB, Uccellini MB, Holtzman MJ, Garcia-Sastre A, Schotsaert M, Diamond MS. 2022. SARS-CoV-2 causes lung infection without severe disease in human Ace2 knock-in mice. J Virol 96:e0151121. https://doi.org/10.1128/JVI.01511-21
10. Sun SH, Chen Q, Gu HJ, Yang G, Wang YX, Huang XY, Liu SS, Zhang NN, Li XF, Xiong R, Guo Y, Deng YQ, Huang WJ, Liu Q, Liu QM, Shen YL, Zhou Y, Yang X, Zhao TY, Fan CF, Zhou YS, Qin CF, Wang YC. 2020. A mouse model of SARS-CoV-2 infection and pathogenesis. Cell Host Microbe 28:124–133. https://doi.org/10.1016/j.chom.2020.05.020
11. Bao L, Deng W, Huang B, Gao H, Liu J, Ren L, Wei Q, Yu P, Xu Y, Qi F, et al. 2020. The pathogenicity of SARS-CoV-2 in hACE2 transgenic mice. Nature 583:830–833. https://doi.org/10.1038/s41586-020-2312-y
12. Jiang RD, Liu MQ, Chen Y, Shan C, Zhou YW, Shen XR, Li Q, Zhang L, Zhu Y, Si HR, Wang Q, Min J, Wang X, Zhang W, Li B, Zhang HJ, Baric RS, Zhou P, Yang XL, Shi ZL. 2020. Pathogenesis of SARS-CoV-2 in transgenic mice expressing human angiotensin-converting enzyme 2. Cell 182:50–58. https://doi.org/10.1016/j.cell.2020.05.027
13. Winkler ES, Bailey AL, Kafai NM, Nair S, McCune BT, Yu J, Fox JM, Chen RE, Earnest JT, Keeler SP, Ritter JH, Kang LI, Dort S, Robichaud A, Head R, Holtzman MJ, Diamond MS. 2020. SARS-CoV-2 infection of human Ace2-transgenic mice causes severe lung inflammation and impaired function. Nat Immunol 21:1327–1335. https://doi.org/10.1038/s41590-020-0794-2
14. Zheng J, Wong L-YR, Li K, Verma AK, Ortiz ME, Wohlford-Lenane C, Leidinger MR, Knudson CM, Meyerholz DK, McCray PB Jr, Perlman S. 2021. COVID-19 treatments and pathogenesis including anosmia in K18-Hace2 mice. Nature 589:603–607. https://doi.org/10.1038/s41586-020-2943-z
15. Sun J, Zhuang Z, Zheng J, Li K, Wong R-Y, Liu D, Huang J, He J, Zhu A, Zhao J, et al. 2020. Generation of a broadly useful model for COVID-19 pathogenesis, vaccination, and treatment. Cell 182:734–743. https://doi.org/10.1016/j.cell.2020.06.010
16. Israelow B, Song E, Mao T, Lu P, Meir A, Liu F, Alfajaro MM, Wei J, Dong H, Homer RJ, Ring A, Wilen CB, Iwasaki A. 2020. Mouse model of SARS-CoV-2 reveals inflammatory role of type I interferon signaling. J Exp Med 217:12. https://doi.org/10.1084/jem.20201241
17. Hassan AO, Case JB, Winkler ES, Thackray LB, Kafai NM, Bailey AL, McCune BT, Fox JM, Chen RE, Alsoussi WB, Turner JS, Schmitz AJ, Lei T, Shrihari S, Keeler SP, Fremont DH, Greco S, McCray PB, Perlman S, Holtzman MJ, Ellebedy AH, Diamond MS. 2020. A SARS-CoV-2 infection model in mice demonstrates protection by neutralizing antibodies. Cell 182:744–753. https://doi.org/10.1016/j.cell.2020.06.011
18. Kumari P, Rothan HA, Natekar JP, Stone S, Pathak H, Strate PG, Arora K, Brinton MA, Kumar M. 2021. Neuroinvasion and encephalitis following intranasal inoculation of SARS-CoV-2 in K18-Hace2 mice. Viruses 13:132. https://doi.org/10.3390/v13010132
19. Wan Y, Shang J, Graham R, Baric RS, Li F, Gallagher T. 2020. Receptor recognition by the novel coronavirus from Wuhan: an analysis based on decade-long structural studies of SARS coronavirus. J Virol 94:e00127–20. https://doi.org/10.1128/JVI.00127-20
20. Wong L-Y, Zheng J, Wilhelmsen K, Li K, Ortiz ME, Schnicker NJ, Thurman A, Pezzulo AA, Szachowicz PJ, Li P, Pan R, Klumpp K, Aswad F, Rebo J, Narumiya S, Murakami M, Zuniga S, Sola I, Enjuanes L, Meyerholz DK, Fortney K, McCray PB, Perlman S. 2022. Eicosanoid signalling blockade protects middle-aged mice from severe COVID-19. Nature 605:146–151. https://doi.org/10.1038/s41586-022-04630-3
21. Leist SR, Dinnon KH, Schäfer A, Tse LV, Okuda K, Hou YJ, West A, Edwards CE, Sanders W, Fritch EJ, Gully KL, Scobey T, Brown AJ, Sheahan TP, Moorman NJ, Boucher RC, Gralinski LE, Montgomery SA, Baric RS. 2020. A mouse-adapted SARS-CoV-2 induces acute lung injury and mortality in standard laboratory mice. Cell 183:1070–1085. https://doi.org/10.1016/j.cell.2020.09.050
22. Roberts A, Deming D, Paddock CD, Cheng A, Yount B, Vogel L, Herman BD, Sheahan T, Heise M, Genrich GL, Zaki SR, Baric R, Subbarao K. 2007. A mouse-adapted SARS-coronavirus causes disease and mortality in BALB/C mice. PLoS Pathog 3:e5. https://doi.org/10.1371/journal.ppat.0030005
23. Sun S, Gu H, Cao L, Chen Q, Ye Q, Yang G, Li R-T, Fan H, Deng Y-Q, Song X, et al. 2021. Characterization and structural basis of a lethal mouse-adapted SARS-CoV-2. Nat Commun 12:5654. https://doi.org/10.1038/s41467-021-25903-x
24. Yan K, Dumenil T, Tang B, Le TT, Bishop CR, Suhrbier A, Rawle DJ. 2022. Evolution of Ace2-independent SARS-CoV-2 infection and mouse adaption after passage in cells expressing human and mouse Ace2. Virus Evol 8:veac063. https://doi.org/10.1093/ve/veac063
25. Li Q, Nie J, Wu J, Zhang L, Ding R, Wang H, Zhang Y, Li T, Liu S, Zhang M, et al. 2021. SARS-CoV-2 501Y.V2 variants lack higher infectivity but do have immune escape. Cell 184:2362–2371. https://doi.org/10.1016/j.cell.2021.02.042
26. Syed AM, Taha TY, Tabata T, Chen IP, Ciling A, Khalid MM, Sreekumar B, Chen PY, Hayashi JM, Soczek KM, Ott M, Doudna JA. 2021. Rapid assessment of SARS-CoV-2-evolved variants using virus-like particles. Science 374:1626–1632. https://doi.org/10.1126/science.abl6184
27. Qing E, Kicmal T, Kumar B, Hawkins GM, Timm E, Perlman S, Gallagher T. 2021. Dynamics of SARS-CoV-2 spike proteins in cell entry: control elements in the amino-terminal domains. mBio 12:e0159021. https://doi.org/10.1128/mBio.01590-21
28. Saito A, Irie T, Suzuki R, Maemura T, Nasser H, Uriu K, Kosugi Y, Shirakawa K, Sadamasu K, Kimura I, et al. 2022. Enhanced fusogenicity and pathogenicity of SARS-CoV-2 delta P681R mutation. Nature 602:300–306. https://doi.org/10.1038/s41586-021-04266-9

29. Suzuki R, Yamasoba D, Kimura I, Wang L, Kishimoto M, Ito J, Morioka Y, Nao N, Nasser H, Uriu K, et al. 2022. Attenuated fusogenicity and pathogenicity of SARS-CoV-2 omicron variant. Nature 603:700–705. https://doi.org/10.1038/s41586-022-04462-1
30. Viner RM, Mytton OT, Bonell C, Melendez-Torres GJ, Ward J, Hudson L, Waddington C, Thomas J, Russell S, van der Klis F, Koirala A, Ladhani S, Panovska-Griffiths J, Davies NG, Booy R, Eggo RM. 2021. Susceptibility to SARS-CoV-2 infection among children and adolescents compared with adults: a systematic review and meta-analysis. JAMA Pediatr 175:143–156. https://doi.org/10.1001/jamapediatrics.2020.4573
31. Team C-R. 2020. Coronavirus disease 2019 in children - United States, February 12-April 2, 2020. MMWR Morb Mortal Wkly Rep 69:422–426. https://doi.org/10.15585/mmwr.mm6914e4
32. Mori H, Obinata H, Murakami W, Tatsuya K, Sasaki H, Miyake Y, Taniguchi Y, Ota S, Yamaga M, Suyama Y, Tamura K. 2021. Comparison of COVID-19 disease between young and elderly patients: hidden viral shedding of COVID-19. J Infect Chemother 27:70–75. https://doi.org/10.1016/j.jiac.2020.09.003
33. Chen Y, Li C, Liu F, Ye Z, Song W, Lee ACY, Shuai H, Lu L, To KK-W, Chan JF-W, Zhang AJ, Chu H, Yuen K-Y. 2022. Age-associated SARS-CoV-2 breakthrough infection and changes in immune response in a mouse model. Emerging Microbes & Infections 11:368–383. https://doi.org/10.1080/22221751.2022.2026741
34. O'Driscoll M, Ribeiro Dos Santos G, Wang L, Cummings DAT, Azman AS, Paireau J, Fontanet A, Cauchemez S, Salje H. 2021. Age-specific mortality and immunity patterns of SARS-CoV-2. Nature 590:140–145. https://doi.org/10.1038/s41586-020-2918-0
35. Zhang Y, Huang K, Wang T, Deng F, Gong W, Hui X, Zhao Y, He X, Li C, Zhang Q, Chen X, Lv C, Lin X, Yang Y, Sun X, Shi Z, Chen H, Zou Z, Jin M, Gallagher T. 2021. SARS-CoV-2 rapidly adapts in aged BALB/C mice and induces typical pneumonia. J Virol 95. https://doi.org/10.1128/JVI.02477-20
36. Gawish R, Maier B, Obermayer G, Watzenboeck ML, Gorki A-D, Quattrone F, Farhat A, Lakovits K, Hladik A, Korosec A, Alimohammadi A, Mesteri I, Oberndorfer F, Oakley F, Brain J, Boon L, Lang I, Binder CJ, Knapp S. 2022. A neutrophil-B-cell axis impacts tissue damage control in a mouse model of intraabdominal bacterial infection via Cxcr4. Elife 11:e78291. https://doi.org/10.7554/eLife.78291
37. Leist SR, Dinnon KH, Schäfer A, Tse LV, Okuda K, Hou YJ, West A, Edwards CE, Sanders W, Fritch EJ, Gully KL, Scobey T, Brown AJ, Sheahan TP, Moorman NJ, Boucher RC, Gralinski LE, Montgomery SA, Baric RS. 2020. A mouse-adapted SARS-CoV-2 induces acute lung injury and mortality in standard laboratory mice. Cell 183:1070–1085. https://doi.org/10.1016/j.cell.2020.09.050
38. Cui X, Chen W, Zhou H, Gong Y, Zhu B, Lv X, Guo H, Duan J, Zhou J, Marcon E, Ma H. 2021. Pulmonary edema in COVID-19 patients: mechanisms and treatment potential. Front Pharmacol 12:664349. https://doi.org/10.3389/fphar.2021.664349
39. Jin JM, Bai P, He W, Wu F, Liu XF, Han DM, Liu S, Yang JK. 2020. Gender differences in patients with COVID-19: focus on severity and mortality. Front Public Health 8:152. https://doi.org/10.3389/fpubh.2020.00152
40. Qi S, Ngwa C, Morales Scheihing DA, Al Mamun A, Ahnstedt HW, Finger CE, Colpo GD, Sharmeen R, Kim Y, Choi HA, McCullough LD, Liu F. 2021. Sex differences in the immune response to acute COVID-19 respiratory tract infection. Biol Sex Differ 12:66. https://doi.org/10.1186/s13293-021-00410-2
41. Peckham H, de Gruijter NM, Raine C, Radziszewska A, Ciurtin C, Wedderburn LR, Rosser EC, Webb K, Deakin CT. 2020. Male sex identified by global COVID-19 meta-analysis as a risk factor for death and ITU admission. Nat Commun 11:6317. https://doi.org/10.1038/s41467-020-19741-6
42. Williamson EJ, Walker AJ, Bhaskaran K, Bacon S, Bates C, Morton CE, Curtis HJ, Mehrkar A, Evans D, Inglesby P, et al. 2020. Factors associated with COVID-19-related death using opensafely. Nature 584:430–436. https://doi.org/10.1038/s41586-020-2521-4
43. Yasui F, Matsumoto Y, Yamamoto N, Sanada T, Honda T, Munakata T, Itoh Y, Kohara M. 2022. Infection with the SARS-CoV-2 B.1.351 variant is lethal in aged BALB/C mice. Sci Rep 12:4150. https://doi.org/10.1038/s41598-022-08104-4
44. Pan T, Chen R, He X, Yuan Y, Deng X, Li R, Yan H, Yan S, Liu J, Zhang Y, Zhang X, Yu F, Zhou M, Ke C, Ma X, Zhang H. 2021. Infection of wild-type mice by SARS-CoV-2 B.1.351 variant indicates a possible novel cross-species transmission route. Signal Transduct Target Ther 6:420. https://doi.org/10.1038/s41392-021-00848-1
45. Li K, Wohlford-Lenane CL, Channappanavar R, Park JE, Earnest JT, Bair TB, Bates AM, Brogden KA, Flaherty HA, Gallagher T, Meyerholz DK, Perlman S, McCray PB. 2017. Mouse-adapted MERS coronavirus causes lethal lung disease in human Dpp4 knockin mice. Proc Natl Acad Sci U S A 114:E3119–E3128. https://doi.org/10.1073/pnas.1619109114
46. Wong L-YR, Zheng J, Wilhelmsen K, Li K, Ortiz ME, Schnicker NJ, Thurman A, Pezzulo AA, Szachowicz PJ, Li P, Pan R, Klumpp K, Aswad F, Rebo J, Narumiya S, Murakami M, Zuniga S, Sola I, Enjuanes L, Meyerholz DK, Fortney K, McCray PB Jr, Perlman S. 2022. Eicosanoid signaling blockade protects middle-aged mice from severe COVID-19. Nature 605:146–151. https://doi.org/10.1038/s41586-022-04630-3
47. Yi C, Sun X, Ye J, Ding L, Liu M, Yang Z, Lu X, Zhang Y, Ma L, Gu W, Qu A, Xu J, Shi Z, Ling Z, Sun B. 2020. Key residues of the receptor binding motif in the spike protein of SARS-CoV-2 that interact with Ace2 and neutralizing antibodies. Cell Mol Immunol 17:621–630. https://doi.org/10.1038/s41423-020-0458-z
48. Weisblum Y, Schmidt F, Zhang F, DaSilva J, Poston D, Lorenzi JC, Muecksch F, Rutkowska M, Hoffmann H-H, Michailidis E, et al. 2020. Escape from neutralizing antibodies by SARS-CoV-2 spike protein variants. Elife 9:e61312. https://doi.org/10.7554/eLife.61312
49. Bader SM, Cooney JP, Sheerin D, Taiaroa G, Harty L, Davidson KC, Mackiewicz L, Dayton M, Wilcox S, Whitehead L, et al. 2023. SARS-CoV-2 mouse adaptation selects virulence mutations that cause TNF-driven age-dependent severe disease with human correlates. Proc Natl Acad Sci U S A 120:e2301689120. https://doi.org/10.1073/pnas.2301689120
50. Kim S, Liu Y, Ziarnik M, Seo S, Cao Y, Zhang XF, Im W. 2023. Binding of human Ace2 and RBD of omicron enhanced by unique interaction patterns among SARS-CoV-2 variants of concern. J Comput Chem 44:594–601. https://doi.org/10.1002/jcc.27025
51. Han P, Li L, Liu S, Wang Q, Zhang D, Xu Z, Han P, Li X, Peng Q, Su C, Huang B, Li D, Zhang R, Tian M, Fu L, Gao Y, Zhao X, Liu K, Qi J, Gao GF, Wang P. 2022. Receptor binding and complex structures of human Ace2 to spike RBD from omicron and delta SARS-CoV-2. Cell 185:630–640. https://doi.org/10.1016/j.cell.2022.01.001
52. Takashita E, Yamayoshi S, Simon V, van Bakel H, Sordillo EM, Pekosz A, Fukushi S, Suzuki T, Maeda K, Halfmann P, Sakai-Tagawa Y, Ito M, Watanabe S, Imai M, Hasegawa H, Kawaoka Y. 2022. Efficacy of antibodies and antiviral drugs against omicron BA.2.12.1, BA.4, and BA.5 subvariants. N Engl J Med 387:468–470. https://doi.org/10.1056/NEJMc2207519
53. Laurini E, Marson D, Aulic S, Fermeglia A, Pricl S. 2021. Molecular rationale for SARS-CoV-2 spike circulating mutations able to escape bamlanivimab and etesevimab monoclonal antibodies. Sci Rep 11:20274. https://doi.org/10.1038/s41598-021-99827-3
54. Starr TN, Greaney AJ, Addetia A, Hannon WW, Choudhary MC, Dingens AS, Li JZ, Bloom JD. 2021. Prospective mapping of viral mutations that escape antibodies used to treat COVID-19. Science 371:850–854. https://doi.org/10.1126/science.abf9302
55. Yan F, Li E, Wang T, Li Y, Liu J, Wang W, Qin T, Su R, Pei H, Wang S, Feng N, Zhao Y, Yang S, Xia X, Gao Y. 2022. Characterization of two heterogeneous lethal mouse-adapted Sars-CoV-2 variants recapitulating representative aspects of human COVID-19. Front Immunol 13:821664. https://doi.org/10.3389/fimmu.2022.821664
56. Rathnasinghe R, Jangra S, Ye C, Cupic A, Singh G, Martínez-Romero C, Mulder LCF, Kehrer T, Yildiz S, Choi A, et al. 2022. Characterization of SARS-CoV-2 spike mutations important for infection of mice and escape from human immune sera. Nat Commun 13:3921. https://doi.org/10.1038/s41467-022-30763-0
57. Ko SH, Bayat Mokhtari E, Mudvari P, Stein S, Stringham CD, Wagner D, Ramelli S, Ramos-Benitez MJ, Strich JR, Davey RT, Zhou T, Misasi J, Kwong PD, Chertow DS, Sullivan NJ, Boritz EA. 2021. High-throughput, single-copy sequencing reveals SARS-CoV-2 spike variants coincident with mounting humoral immunity during acute COVID-19. PLoS Pathog 17:e1009431. https://doi.org/10.1371/journal.ppat.1009431
58. Nakandakari-Higa S, Parsa R, Reis BS, de Carvalho RVH, Mesin L, Hoffmann H-H, Bortolatto J, Muramatsu H, Lin PJC, Bilate AM, Rice CM, Pardi N, Mucida D, Victora GD, Canesso MCC. 2022. A minimally-edited mouse model for infection with multiple SARS-CoV-2 strains. Front Immunol 13:1007080. https://doi.org/10.3389/fimmu.2022.1007080

59. Qing E, Hantak MP, Galpalli GG, Gallagher T. 2020. Evaluating MERS-CoV entry pathways. Methods Mol Biol 2099:9–20. https://doi.org/10.1007/978-1-0716-0211-9_2
60. Qing Enya, Li P, Cooper L, Schulz S, Jäck H-M, Rong L, Perlman S, Gallagher T. 2022. Inter-domain communication in SARS-CoV-2 spike proteins controls protease-triggered cell entry. Cell Rep 39:110786. https://doi.org/10.1016/j.celrep.2022.110786
61. Li K, Wohlford-Lenane C, Perlman S, Zhao J, Jewell AK, Reznikov LR, Gibson-Corley KN, Meyerholz DK, McCray PB. 2016. Middle East respiratory syndrome coronavirus causes multiple organ damage and lethal disease in mice transgenic for human dipeptidyl peptidase 4. J Infect Dis 213:712–722. https://doi.org/10.1093/infdis/jiv499
62. Morin A, Eisenbraun B, Key J, Sanschagrin PC, Timony MA, Ottaviano M, Sliz P. 2013. Collaboration gets the most out of software. Elife 2:e01456. https://doi.org/10.7554/eLife.01456
63. Meyerholz DK, Beck AP. 2018. Principles and approaches for reproducible scoring of tissue stains in research. Lab Invest 98:844–855. https://doi.org/10.1038/s41374-018-0057-0